Additive Manufacturing 30 (2019) 100930

Contents lists available at ScienceDirect

Additive Manufacturing

journal homepage: www.elsevier.com/locate/addma

Full Length Article

Towards digital metal additive manufacturing via high-temperature drop-on-demand jetting

Marco Simonelli[a,*], Nesma Aboulkhair[a], Mircea Rasa[b], Mark East[a], Chris Tuck[a], Ricky Wildman[a], Otto Salomons[b], Richard Hague[a]

[a] Centre for Additive Manufacturing, The University of Nottingham, UK
[b] Océ – A Canon Company, the Netherlands

ARTICLE INFO

Keywords:
Drop-on-demand jetting
Material jetting
Digital manufacturing
Printed electronics
Liquid metal printing

ABSTRACT

Drop-on-demand jetting of metals offers a fully digital manufacturing approach to surpass the limitations of the current generation powder-based additive manufacturing technologies. However, research on this topic has been restricted mainly to near-net shaping of relatively low melting temperature metals. Here it is proposed a novel approach to jet molten metals at high-temperatures (> 1000 °C) to enable the direct digital additive fabrication of micro- to macro-scale objects. The technique used in our research – "MetalJet" - is discussed by studying the ejection and the deposition of two example metals, tin and silver. The applicability of this new technology to additive manufacturing is evaluated through the study of the interface formed between the droplets and the substrate, the inter-droplets bonding, the microstructure and the geometrical fidelity of the printed objects. The research shows that the integrity of the samples (in terms of density as well as metallurgy) varies dramatically in the two investigated materials due to the different conditions that are required to melt the interface of the stacked droplets. Nevertheless the research shows that by a careful choice of the jetting strategy and sintering treatments 3D structures of various complexity can be formed. This research paves the way towards the next generation metal additive manufacturing where various printing resolutions and multi-material capabilities could be used to obtain functional components for applications in printed electronics, medicine and the automotive sectors.

1. Introduction

Mirroring the Drop-on-Demand (DoD) benefits of conventional polymeric 2D and 3D ink-jetting, DoD jetting of fully melted liquid metallics conceptually gives a promising approach for the production of both 2D and 3D constructs. The attractiveness of DoD liquid metal "3D printing" lies within its simple workflow, as structures can be created through the digitally-driven, on-demand deposition of discrete volumes of metals, as opposed to the complex handling of metallic powders intrinsic to all other conventional powder-bed fusion, binder-jetting or powder-feed-based Additive Manufacturing (AM) techniques [1]. Additionally, DoD jetting-based techniques are inherently scalable and give the newly-offered potential to shape functional parts made of dissimilar materials [2,3], that is in stark contrast to conventional single-material metallic AM systems. However, to date, both research and industrial implementation of metallic DoD jetting has been confined to relatively low-temperature (< 700 °C) alloys in large droplets (> 200 µm, typically > 500 µm), leading to near-net structures requiring post-process machining rather than net-shapes that can be used directly [4–11]. Key to DoD liquid metal 3D printing is the generation and control of a stable stream of metallic droplets. Various jetting techniques have been presented in the literature. Ejection through piezoelectric actuation, perhaps the most common form of actuation, is limited by the operating temperature of the piezoelectric crystal and therefore has only been used for printing particulate-loaded carrier inks, where the carrier ink is evaporated post deposition and the particulates (which are ~1 µm in size) are then furnace processed to sinter them together [12,13], low melting point metals (tin, gallium, indium and their alloys) and other eutectics [4,5,14,15]. The use of plunger rods to shield the piezoelectric crystals from the molten metal has also been proposed to extend the number of printable metals by piezoelectric actuation resulting in the successful jetting of metals with relatively higher melting point such as aluminum alloys [16]. By having no moving parts in direct contact with the molten metal but inert gas, pneumatic actuation has been shown to overcome the temperature limitation of the piezoelectric ejection [7,17]. Pneumatic actuation is

* Corresponding author at: Advanced Manufacturing Building, Jubilee Campus, University of Nottingham, NG8 1BB, Nottingham, UK.
E-mail address: Marco.Simonelli@nottingham.ac.uk (M. Simonelli).

https://doi.org/10.1016/j.addma.2019.100930
Received 19 September 2019; Received in revised form 28 October 2019; Accepted 29 October 2019
Available online 31 October 2019

however typically characterized by low printing resolution (mm scale) due to the relatively low response rate of the actuators and the consequent generation of large droplets, and its use for precision manufacturing and in miniaturization of printed electronics remains uncertain [8,9]. Finally MagnetoHydroDynamic (MHD) actuation, another non-contact actuation technique where metal flow is generated by the application of an electromagnetic force, has led to successful printing of structures in a number of relative low melting temperature metals [10,11]. Recently, interesting developments have been reported in the printing of a number of Al alloys [18–20], where magnetic pressure is used to constrict liquid metals inside a crucible and directly control the corresponding outflow from a nozzle orifice. Using this promising technique, a number of near-net shapes have been produced showing the potential advantages associated to liquid metal printing AM [21]. To advance the current state-of-the-art we have developed a novel DoD metal jetting technique, MetalJet [22], capable of depositing micro-droplets of high-temperature metals (< 80 µm droplet diameter and > 1000 °C melt point) to form arbitrary *net-shape* 3D constructs requiring no post-process machining. In this research, we aim to explain how this simple approach can lead to the production of structures of various complexity unveiling both the technical and materials science challenges associated to this approach to manufacturing.

2. Materials and methods

2.1. Materials

The printing materials were Sn and Ag grade 5 N supplied by ESPI Metals in the form of shots and rods, respectively. The substrates used for printing were Cu plates (99.9%) supplied by Goodfellow, UK except for the case of 1) the tracks printed for electrical resistivity measurement, where Cu plates were coated by a commercial Cu ink solution (Promethean Particles Ltd, UK) and 2) the Ag samples printed for sintering, where Al_2O_3 substrates were used (CSC Ceramics, UK). For sintering treatments, Al_2O_3 substrates were used as Ag and Cu form an eutectic alloy at approx. 780 °C so any sintering treatments above this temperature would cause a collapse and dissolution of the entire structure. In addition Al_2O_3 was also chosen as it generally accepted that ionocovalent structures (where oxygen ions form a hexagonal close-packed structure with aluminium ions filling two-thirds of the octahedral interstices) might facilitate diffusive bonding with metals that possess great affinity to oxygen.

2.2. Jetting process

Fig. 1(a) shows the working principle of the MetalJet technology used in this research [22].

Under an argon protective atmosphere, desired metals (Sn or Ag in the present study) are melted in distinct cartridges by induction heating. Each cartridge's ejecting chamber is surrounded by permanent magnets, which are used to generate a static magnetic field B perpendicular to the flow of the molten metal (magnetic flux of constant intensity of 2 T). The temperature of the molten metal is inferred by measuring the temperature on the nozzle plate (orifice-end) by pyrometry (Sensortherm GmbH). At the tip of the ejecting chamber, the molten metal is also directly in contact with tungsten electrodes that are used to pass spikes of electrical current provided by a programmable current source. The shape and duration of the current pulses were controlled by a waveform generator (Agilent Technologies, 33220A) and then amplified by current amplifiers (ServoWatt DCP780/30A). Exploiting the Lorentz force principle, a push force can be thus exerted on the molten metal to generate metal droplets on-demand (Fig. 1 (b–e)). In this configuration, the droplet size and speed are controlled by the nozzle orifice geometry (length and diameter), the magnetic field intensity and the amplitude and duration of the sustained electrical current. The nozzle geometry and the scale of the jetting parameters were designed considering a target printing resolution of ≈ 50 µm, i.e. the typical resolution of modern printed electronics [23], but it is noteworthy that this approach is flexible to generate droplets of smaller or larger diameter, if required. As captured in more detail in Video 1, the formation of the droplets occurs in three consecutive events: 1) the molten metal is firstly accelerated through the nozzle orifice to form a jet, 2) a droplet is obtained from the breaking of the jet tail and 3) the remaining tail retracts into the nozzle ready for a new jetting sequence. As the meniscus in the nozzle varies depending on the jetting temperature, wettability and impurities, tuning the actuation pulse is essential at the beginning of each printing experiment. During this initial phase, the amplitude of the current pulse was typically varied between 20 and 120A until the meniscus head of the liquid metal reached the tip of the nozzle with a typical velocity of 1 m/s. Meniscus with lower inertia protrude outside of the orifice but never detach from the nozzle. Adjusting the pulse duration, it was then possible to control the volume of jet (and therefore that of the droplet) as well as the length of its tail. The jetting pulse shape was thus optimized to control the break off of the jet tail and to allow molten metal to detach without secondary satellites. As the jet snaps off, it quickly shapes into a droplet by surface tension with the remaining tail being retracted into the orifice in the equilibrium position by capillary action. At this stage of the research, the parameters vary for each jetting and printing experiment. Research is currently ongoing [33] to establish the exact physics of the jetting process (particularly at high temperatures above 1000 °C) and establish general jetting protocols. The jetting process (droplet formation, droplet speed, radius and trajectory) was monitored by a JetXpert dropwatcher, which enabled droplet stroboscopic backlighting synchronous to the firing of the print-head.

2.3. Tuning of the jetting process

To assess the typical printing accuracy of the process, the droplet jetting stability at an ejection rate of 500 Hz was assessed by

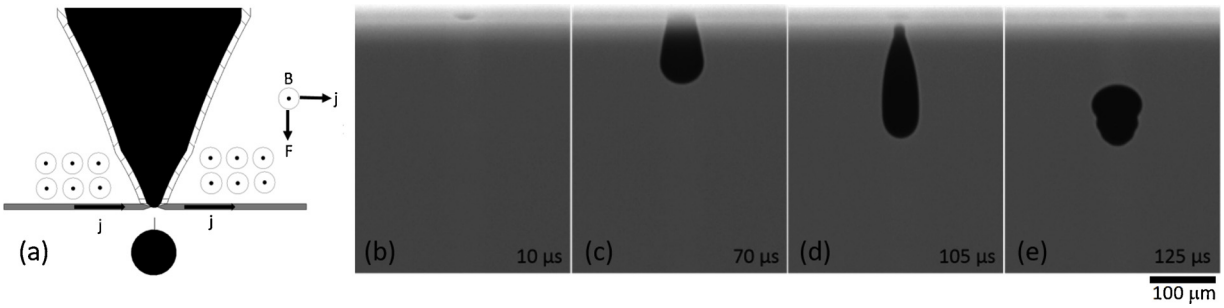

Fig. 1. The MetalJet ejection mechanism. (a) Jetting by magnetohydrodynamics (MHD): the directions of the current density j and the Lorentz force, F, acting on the metal are indicated in the diagram by black arrows. The direction of the perpendicular magnetic field B (pointing out of the screen) is indicated by the concentric circles. As an example, snapshots of the formation of Ag droplets are shown after (b) 10 µs ; (c) 70 µs; (d) 105 µs and (e), 125 µs from the start of the MHD actuation.

Table 1
Sn and Ag jetting stability: droplet speed, radius and trajectory.

		Sn	Ag
Average droplet speed v_j	[m/s]	1.72	1.88
Speed deviation σ_{v_j}	[m/s]	0.01	0.04
Average trajectory	[°deg]	90.3	89.9
Angle deviation ϑ	[°deg]	0.13	0.2
Average radius r	[μm]	39	38

continuously measuring the in-flight droplet radius, speed and trajectory until feedstock depletion (Table 1).

For both Sn and Ag, the deviation from the average droplet radius is comprised within 10% although it should be noted that the measurement of the droplet radius is subject to artefacts that occur due to changes in the in-flight droplet morphology and therefore the results cannot be quantitatively discussed. The deviation from the average speed and trajectory is comprised within 11% and ~ 1% for Ag and 4% and ~ 1% for Sn, respectively. Nevertheless these instabilities are lower than those reported in the literature for solder jetting, causing positional inaccuracy comparable to that of typical office inkjet printers. The misplacement of a droplet due to an angular deviation from the ideal perpendicular jet, δ_ϑ, can indeed be calculated as $\delta_\vartheta = d \times \tan\vartheta$, where d is the nozzle-substrate distance and ϑ is the deviation from the perpendicular jet. For small angular deviations (as in the present case) $\delta_\vartheta \sim d \times \vartheta$. For $d = 1$ mm, we obtain $\delta_\vartheta \sim 2.3$ μm (Sn) and $\delta_\vartheta \sim 3.5$ μm (Ag). The misplacement of a droplet due to variations in the droplet speed, δ_v, can instead be calculated as $\delta_v = \frac{v_s \times d}{v_j^2} \times \sigma_{v_j}$ where v_s is the stage speed, d is the nozzle-substrate distance and v_j and σ_{v_j} are the average and standard deviation of the droplet speed. At a jetting frequency of 500 Hz and $d = 1$ mm, the positional error caused by the variation in the droplet speed is $\delta_v \sim 0.1$ μm (Sn) and $\delta_\vartheta \sim 0.5$ μm (Ag). The combined total positional accuracy uncertainty is below 4 μm for both metals. The presented equipment is a research platform that is not optimized for printing speed or cost. Nevertheless, by considering the current capabilities a realistic deposition rate up to 2 cm^3/hour per print head can be achieved. However, the deposition rate clearly scales with the volume of the jetted droplets, the building block of our 3D parts. With the necessary changes in the nozzle geometry, it would be straightforward to jet larger droplets and increase the deposition rate dramatically, as per target requirements.

2.4. Printing setup

Droplets were sequentially jetted from stationary print heads onto a substrate mounted on a movable stage (PRO225LM and ANT130-L Aerotech stages for the x-, z- and y-axes, respectively) with a nozzle to substrate distance of 1 mm. A LabVIEW program was used to read the stack of bitmaps corresponding to the printing structure and coordinate the printing process. First, each bitmap was scanned line by line to inform the x- and y-stages on the desired path to follow - the x- and y-axes substrate movements were controlled by simply converting the black pixels of the desired bitmaps into coordinates so that the droplet pitch matched the bitmap resolution. The program then synchronizes the jetting of each droplet with the position of the substrate: droplets are jetted on the basis of the pixel value and substrate speed is directly derived from the desired jetting frequency and droplet pitch. At the end of each layer, the substrate is lowered (z-axis) by the dictated thickness of the deposit before printing the following layer/bitmap.

2.5. Resistivity measurements

The electrical resistivity of the printed Sn was calculated using the relationship $\rho = (A/L)R$ where ρ is the resistivity to be calculated, R is the resistance of the printed track (measured experimentally), and A and L are the cross-sectional area and length of the track, respectively. Two-layer tracks with a length of 40 mm were printed on a Al_2O_3 plate coated with un-sintered Cu ink to ease the detachment of the printed structure prior to measurement. The dimensions of the tracks where calculated by microscopy analysis. The resistance of the tracks was measured using a Hameg LCR high precision meter (HM 8018). The reported values are an average of the electrical resistivity of five different tracks.

2.6. Microscopy and metrology analysis

The 3D structures where examined using a FEI Quanta 200 3D Dual Beam FIB-SEM. The same microscope was also used to section the droplets and expose the interfaces formed in the structures. The microstructure of such interfaces was studied using a FEI Tecnai F20 TEM operated at 200 kV. Porosity was characterized by X-Ray Computed Tomography (CT) carried out on a Zeiss Xradia Versa XRM-500 system (voxel size 1 μm). The rendering of the porosity was performed using the software Avizo Fire 9.0.1. The comparison of the physical dimensions of example printed specimens with those of the corresponding digital models was used to assess the printing accuracy that can be achieved by this AM approach. A CAD cuboid structure of 10 × 2 x 3 mm (*x*-,*y*- and *z*-) was prepared and then converted to a stack of bitmaps at a resolution corresponding to a suitable droplet pitch, 363 and 338 for Sn and Ag, respectively. The CAD was sliced at a layer thickness of 40 μm – this being the typical thickness of droplets deposited on the same printing substrates in previous experiments. The dimensional accuracy of the printed parts was examined using the same FIB-SEM and a focus-variation 3D microscope (Alicona Infinite Focus G5).

3. Results and discussion

3.1. Additive manufacture of 3D structures in Sn

To demonstrate the printing capabilities associated with the MetalJet approach various structures in Sn were fabricated to allow the study of how objects are made one droplet at the time (Fig. 2).

Fig. 2(a) shows a lateral view of a single Sn droplet deposited on a Cu substrate. Upon contact with the substrate, the liquid Sn spreads driven by the dynamic pressure of the impact and then solidifies bottom up. The oscillations of the melt due to the balancing of inertial and capillary forces can be observed in the form of surface ripples that have frozen as the solidification front sweeps the entire droplet [24,25]. As the metal is deposited gently (Weber number, $2.6 < We < 4.6$) and in a superheated state, its flow is essentially unaffected by the viscosity (Ohnesorge number, $Oh < < 0.1$) [26]. Due to the metallic compatibility of Cu and Sn, the droplet realizes a strong bonding with the substrate. Fig. 2(b–c) shows the interface formed by the Sn droplet on the substrate. The TEM investigation indicates that the liquid Sn reacts with the substrate material to form an interface consisting of two intermetallics (ε-Cu_3Sn and η-Cu_6Sn_5), as predicted by the Sn-Cu phase diagram. The layered interface suggests that ε-Cu_3Sn forms in the first stage of the solidification when Sn is in direct contact with Cu,: η-Cu_6Sn_5, appearing with the typical scallop morphology [27], would instead grow in the latter stages of the solidification at the expense of ε-Cu_3Sn and liquid Sn. The chemical reaction at the interface promotes a strong adhesion of the droplets to the substrate. Continuous tracks made of conjoined droplets were then realised (Fig. 2(d)), where impinging droplets partially re-melt and create a metallurgical bond with the previously deposited droplets. The printing accuracy combined with jetting of droplets of small diameter makes possible the printing of interconnects with high routing density and desired geometries. In Fig. 2(e), it is achieved a routing density of 80 μm, approaching that of the state-of-the-art printed circuit board (typically 50 μm [23]). The electrical resistivity was 1.79 (Ω ·m) and is higher than bulk Sn (1.17 Ω

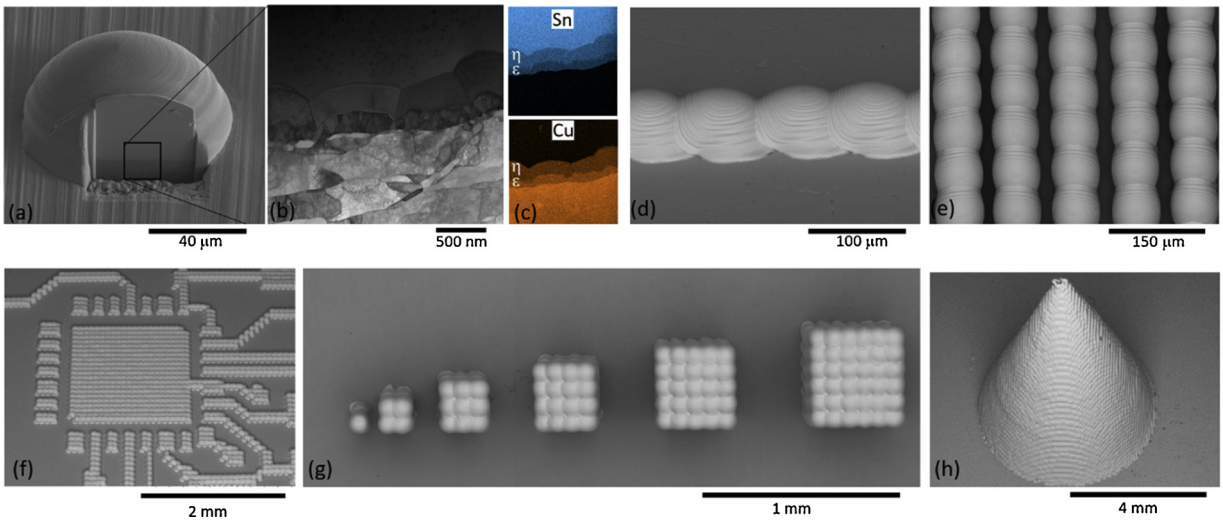

Fig. 2. Sn structures fabricated with the MetalJet technology: (a) side-view of a single Sn droplet. The Sn droplet is sectioned to expose the interface formed with the Cu substrate. The morphology and the element distribution at the interface, with Sn indicated in blue and Cu in orange are shown in (b) and (c), respectively; (d) side-view of droplets sequentially deposited to form a continuous track; (e–f) top-view of tracks closely spaced to achieve high routing density and complex layouts, respectively; (g) top-view of high-aspect pillars of variable cross-sections spaced at intervals multiples of the droplet pitch; (h) example of 3D structure printed in one iteration (For interpretation of the references to colour in this figure legend, the reader is referred to the web version of this article.).

·m), potentially due to small porosity by gas entrapment between contacting droplets or geometrical inaccuracies. However, as the resistivity is one or more order of magnitude lower than that reported for inkjet printing of nano-particle inks, the approach presented here could have a significant importance in electronics [23]. Fig. 2(f–g) shows tracks of variable width and geometrical patterns of various complexity. The structures shown in Fig. 2(d–h) are printed precisely with no satellites or wrongly-positioned droplets that could compromise the function of the patterns. As opposed to other printing techniques [28,29], there is no significant deformation caused by excessive re-melting of the structures demonstrating that this approach can be used to print, for example, fully functional 2D and 3D structures for electronics, where these could be customized circuit layouts or out-of-plane interconnects for stacked 2D electronics, or indeed, complete 3D electronics. Another area of application could be that of selective coatings where the jetting material is deposited to cover selective areas of a planar or non-planar substrate. The printed structures have excellent macroscopic geometrical fidelity to the original digital models, and high density (above 99.9%, Video 2) with a surface texture that favorably compares to that typically obtained with powder-based metal AM (Section 3.3). It was observed that Sn samples exhibit an irregular grain structure characterized by fine and large grains, as shown in Fig. 3. The complex grain structure derives from thermal cycle experienced by the sample during MetalJet. Although each individual droplet cools down rapidly after the impact with the substrate, the sample is held at 170 °C and each droplet re-melts (locally) a portion of the structure. This creates the conditions for grain growth where fine grains of similar orientation are progressively coalescing into larger ones.

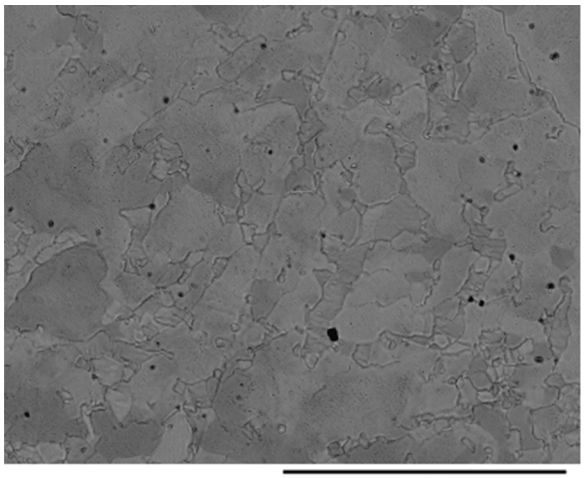

Fig. 3. Backscatter SEM image showing the irregular grain structure in as-deposited Sn samples.

3.2. Additive manufacture of 3D structures in Ag

Next, the capability of the MetalJet system to print high temperature metals (jetting above 1000 °C) are demonstrated by fabricating structures of different geometries in pure Ag (Figs. 4 and 5).

The spreading and solidification of Ag droplets (Fig. 4(a)) are markedly different from those in the case of Sn despite a similar Weber number ($1.7 < We < 3$). Following impact, limited material flow is observed. The solidification fronts are faint and only visible in the top part of the Ag droplets indicating that the droplets possess high viscosity at the time of landing, likely due to rapid cooling after ejection. Solidification thus occurs instantaneously as droplets are pulled inwards by the surface tension. Droplets are loosely attached to the substrate as the interface formed with the Cu substrate is porous and consists of a thin (< 200 nm) layer of Ag supersaturated in Cu, above which, a two-phase Ag + Cu forms (Fig. 4(b–c)). As Ag-Cu are almost completely immiscible below 375 °C [30], no intermetallic compounds form at the interface. Areas where sulfidation has occurred were also observed, likely originating from a high temperature reaction of sulphide species present in the shielding gas with Ag and Cu (Fig. 4(b)). This sharp interface is fragile so Ag structures can be easily detached from the substrate as opposed to that observed in Sn. By comparing the results obtained in Sn and Ag it can be noticed that simple metallurgical rules on metal miscibility can guide the selection of the substrate to realize various degrees of bonding with the impinging droplets. As it can be observed in Fig. 4(d), the viscosity of the Ag droplets affects the droplet packing in contiguous structures. No evident re-melting of the droplet's interface was observed (Fig. 4(e)). As shown in the cross-section of Fig. 4(e), the integrity of the structure depends on the interlocking obtained through the droplets overlap and inter-droplet voids are present in the structures. This is predominantly due to the fact

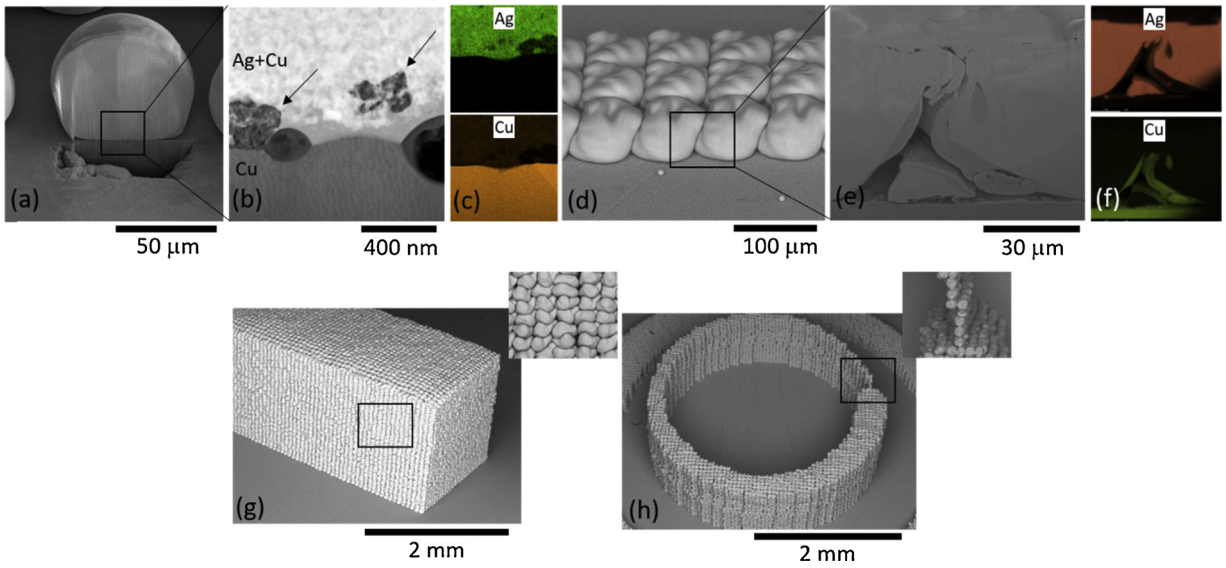

Fig. 4. Ag structures fabricated with the MetalJet technology: (a) side-view of a single Ag droplet. The Ag droplet is FIB-sectioned to expose the interface formed with the Cu substrate. The morphology and the element distribution in the interface, with Ag indicated in green and Cu in orange are shown in (b) and (c), respectively (areas of sulfidation are indicated by black arrows); (d) side-view of droplets sequentially deposited to form continuous tracks; (e–f) inter-droplet interface showing lack of metallurgical bonding and surface composition of Ag droplet following solidification on the substrate; (g–h) examples of 3D geometries printed in Ag (details of structures are shown in the insets) (For interpretation of the references to colour in this figure legend, the reader is referred to the web version of this article.).

that at landing, the heat content in the droplets is not sufficient to melt other portions of the deposited structure (Appendix A) [31]. The section across adjacent Ag droplets shows Cu-rich films on the surface of the droplet (Fig. 4(f)) developing during the spreading and recoiling of the droplets, with molten Ag effectively peeling the upper layer of the Cu substrate. However, it could achieved consistent droplets stacking and the printing of 3D "green" structures with high precision (Fig. 4(g–h)) with average density ~92% and surface roughness of 5.98 µm (Section 3.3). In Fig. 4(g–h) for example, it is demonstrated the printing of solid and hollowed 3D structures with variable diameters and wall thicknesses (from one to eight droplets, as shown in the inset of Fig. 4(h)). In contrast to the tubular structures presented in the literature [28] there is no bulging or loss of dimensional accuracy of the structure due to progressive heating of the deposit as it is being printed, regardless of the sizes of the features that are created. Exploiting the DoD concept, alternative deposition strategies to increase the droplet packing in the structures were then investigated. In Fig. 5, it is reported a deposition strategy where droplet pitch is kept constant but an arbitrary positive and negative offset at the beginning of each line is introduced (in this example it was chosen an offset equal to half the droplet pitch) to print a section of a propeller. This printing strategy increases the droplet-to-droplet contact to promote sintering during post-printing heat treatments. The metallurgical bonds between droplets formed during the post sintering process (Fig. 5(b–c)) strengthen the printed parts providing with better structural integrity, allowing the manipulation and use of the printed objects. Whilst the sintering treatment allows neck growth between droplets, the overall structure retains its geometrical identity. It can be expected that prolonged sintering times could be beneficial to further densification of the structures and we are currently investigating the effect of the sintering regimes and droplet surface composition on the material transport across the droplet surface [32].

The fragile nature of the Ag sample in the as-printed state made the metallurgical preparation of the specimens challenging. Nevertheless, droplets present minimal surface texture and therefore it was possible to assess, at least qualitatively, the grain structure by channeling contrast imaging (Fig. 6). It can be observed that droplets consist of several small grains (Fig. 6(a)) as could be expected considering the relatively rapid cooling rate imposed by the printing process. Noteworthy is also

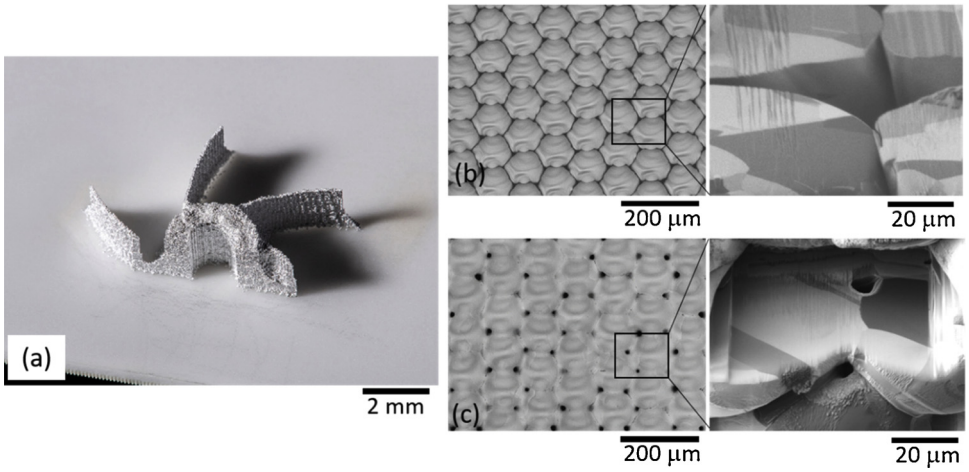

Fig. 5. Example of alternative deposition strategy to promote sintering in post-printing heat treatments. (a–b) section of a Ag propeller and corresponding droplet-to-droplet contact in the as-printed condition; (c) droplet-to-droplet contact after a sintering treatment conducted at 850 °C for 10 h.

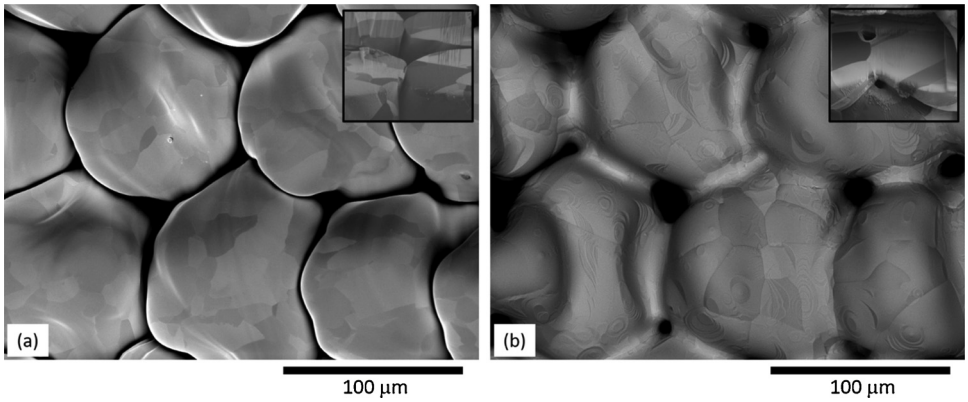

Fig. 6. Grain structure in silver samples in the (a) as-deposited and (b) sintered conditions. The corresponding insets show the interface between contiguous droplets. Following the sintering treatment, droplets are metallurgically bonded.

the morphology of the grains: the grain structure does not appear to be affect by the droplet deposition sequence as no apparent elongation in the grain structure along the droplet lines is observed. As expected, the grain structure coarsens significantly following sintering treatments (Fig. 6(b)). The interface between contiguous droplets is shown in the insets of Fig. 6. No inter-droplet metallurgical bond is observed in the as-deposited Ag sample (inset of Fig. 6(a)). Following the sintering treatment grain continuity across the interface is observed and droplets are metallurgically joined one another (inset of Fig. 6(b)).

The porosity and the droplet-to-droplet necking in the as-deposited and sintered (930 °C for 6 h) Ag samples was assessed by high-resolution X-Ray CT (Fig. 7). The 3D tomography data are shown in Video 3 and 4. CT data shows that the volume fraction of voids in the samples is not affected by the sintering treatment (average porosity ~ 8% for both conditions). The morphology of porosity however changes significantly. In the as-deposited conditions irregular elongated porosity is observed likely originated from the inter-droplet gaps. As a result of the sintering process and the development of droplets necks, pores assume a spherical and rounded shape. These results emphasize that in order to achieve parts with high density further research efforts have to be spent to tune the dynamics of the droplet impacts- at present capillary driven and hence not permitting Ag to fill the inter-droplet spacing- and on the choice of deposition strategies that enable maximum droplet packing.

3.3. Macroscopic geometric fidelity to the original digital model

The dimensions of the corresponding printed specimens are reported in Table 2.

The results show a tolerance for the x- and y- dimensions of the parts comprised within 0.3% while it was observed a relatively larger deviation from the CAD z-height with the real average layer thickness being ~ 38 and ~ 45 µm for Sn and Ag, respectively. Further research is needed to establish the correlation between jetting parameters (jet temperature and jet exit velocity), substrate properties and the average height splat for the materials, as this will be crucial for printing accurate structures beyond extruded profiles and, in future, components made of multiple materials. The surface texture of the same parts was also analyzed according to the ISO 4287 with a sample and cut off length equal to 1.51 and 0.25 mm, respectively. The average roughness amplitude parameters measured from the top and side surfaces of the parts are reported in Table 3 and indicate the roughness at the macroscale (as opposed to the roughness generated by the solidification ripples present on the surface of the droplets).

The significant difference between the surface roughness of the Sn and Ag is explained by the different drop-on-drop behavior of the materials, with Sn forming droplet metallurgical bonds whilst Ag stacking without significant fusion.

Table 2
Geometrical fidelity of the printed Sn and Ag specimens.

	CAD [mm]	Sn structure [mm]	Ag structure [mm]
x	10.00	10.02	10.01
y	2.00	2.01	2.03
z - 45 layers	1.80	1.71	2.03

4. Conclusions

In summary, this research presents the MetalJet technology as a novel digital fabrication technique to form structures that extend in the macroscale with a lateral resolution of 80 µm (approximately double the accuracy achievable with laser powder-bed AM techniques) in low-

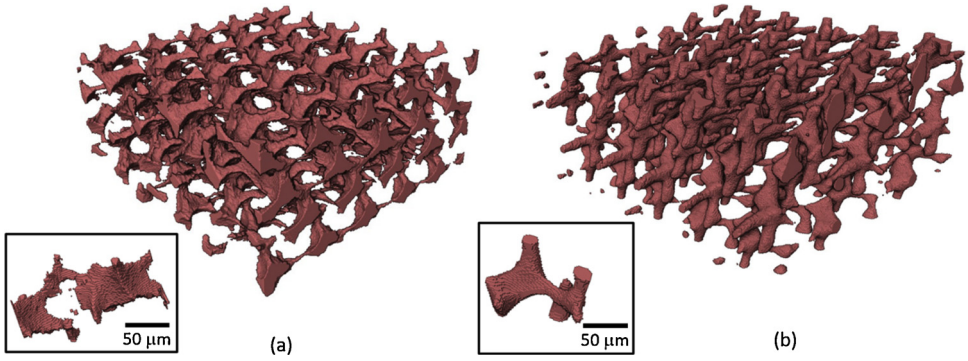

Fig. 7. Reconstructed porosity (in red) from X-Ray CT in (a) as-built and (b) sintered Ag sample. The sintering treatment causes a change of the morphology of the voids as shown in the image insets (For interpretation of the references to colour in this figure legend, the reader is referred to the web version of this article.).

Table 3
Surface roughness parameters Rt and Ra of the Sn and Ag cuboid structure (ISO 4287).

	xy-plane (Sn)	xz-plane (Sn)	xy-plane (Ag)	xz-plane (Ag)
Ra [μm]	1.60	0.39	5.98	n/a
Rt [μm]	7.98	3.43	30.21	n/a

and (relative) high-melting temperature metals. This research has shown the importance of the substrate choice to realize different levels of adhesion and sintering treatments. The temperature range in which metals are miscible, for example, can be used as a guideline to assess whether droplets will form a strong adhesion or a fragile interface. The strength and density of the printed objects can be directly correlated to the droplet bonding. This is a function of the temperature of the droplet interface, and as such liquid metal printing of solid structures in high melting point metals poses significant technological challenges. Nevertheless the DoD approach presented in this study allows the creation of precise "green" structures via deposition strategies that allow high packing density and promote sintering during post-process heat treatments. Various structures were realized by simply co-ordinating the droplet ejection to the movements of a X,Y,Z stage: by extension, additional axis of movement, for example a rotational axis perpendicular to the droplet trajectory, could enable the production of filigree structures, such as winding coils, helixes and mesh tubular structures for electronics and medical applications. Additionally, with further development of the hardware aimed at increasing the temperature of the droplets at landing/substrate and as more jetting materials will be developed we expect to extend the capabilities of the MetalJet fabrication towards the printing of a variety of objects made of single and dissimilar materials to fulfil the needs of the next generation additive manufacturing.

Declaration of Competing Interest

The authors declare no conflict of interest.

Acknowledgement

The authors would like to thank the colleagues Martin Hack (Océ-A Canon Company), Ralph Pohl and Bas Lemmon (Demcon Advanced Mechatronics) for their technical support in setting up the printing platform. The authors are grateful to EPSRC for funding the MetalJet printing platform EPSRC (grant referenceEP/P031684/1). Authors declare no competing interests. All data is available in the main text or the appendix.

Appendix A

In-flight droplet cooling and re-melting of the previously deposited material

The metal droplets are jetted superheated above their liquidus temperatures and therefore are subject to rapid convective and radiative cooling during the in-flight phase. As per the small Biot number, the heat conduction in the interior of the droplet can be neglected. Assuming no significant heating by radiation from the nozzle of the cartridge, the droplet cooling during the time of flight can be expressed in the form of the Eq. (A.1):

$$\rho c \frac{4}{3}\pi r^3 \frac{dT}{dt} = -4\pi r^2 \lfloor h(T - T_{amb}) + \varepsilon\sigma(T^4 - T_{amb}^4) \rfloor, \; T(t=0) = T_{drop} \tag{A.1}$$

where ρ is the density of the liquid metal, c is the specific heat capacity of the liquid droplet material, r is the droplet radius, T_{drop} is the droplet temperature at ejection, T_{amb} is the argon gas temperature, h is the heat transfer coefficient, ε and σ are the emissivity and Stefan–Boltzmann constant, respectively. As in the liquid phase there is only a minor variation with temperature of the specific heat c and density ρ it is assumed, for sake of simplicity, constant c and ρ during the cooling of the droplets (Table A1). The convective heat transfer coefficient h was calculated using the relationship $h = \left(\frac{Nu \times k}{D}\right)$, where Nu is the Nusselt number (the gas velocity is assumed to be equal to that the average droplet velocity), k is the thermal conductivity of Ar at the temperature in proximity to the print heads (measured by placing a thermocouple in proximity of the nozzle), D is the average diameter of the droplets. As the process occurs in inert atmosphere, it is assumed a constant value of the emissivity ε associated to the surface of non-oxidised droplets in the liquid state (Table A1).

A finite difference method was used to numerically solve Eq. (A.1), with a step size of 0.0001. With the typical time-of-flight of 1 ms and the jetting temperature used in these experiments the temperature of the Sn and Ag droplet just before impact varies between $595 < T < 615$ °C and $1015 < T < 1025$ °C, respectively.

The re-melting of the previously deposited material and therefore the occurrence of metallurgical bonding is modelled as a two-phase one-dimensional Stefan melting problem [31].

This model considers only the first few instants after the droplet impact ($t < 10\mu s$) and is valid when the characteristic length scale for the thermal conduction in the droplet ($\sim \sqrt{\alpha t}$) is much inferior than the droplet diameter as is the case in our research. This allows to conceptualize the problem as a one-dimensional heat transfer condition between two semi-infinite bodies at different temperature suddenly brought in contact. The droplet spreading does not affect the heat transfer considered in the model and it is assumed that the characteristic length scale for thermal conduction much shorter than the droplet spreading time. Assuming that the dominant heat transfer mode is by conduction through the solid substrate and ideal heat transfer coefficient h at the liquid/solid interface for constant thermo-physical properties, the temperature distribution in the liquid and solid phases is governed by the following equations:

Table A1
Properties of Sn, Ag and Ar at printing conditions.

	Sn	Ag
Density of liquid ρ [kg/m^3]	6714	9320
Specific heat c [J / Kg K]	235	310
Radiation coefficient ε	0.05	0.05
Temperature of Ar gas T_{amb}[K]	443.15	873.15
Thermal conductivity k_{Ar} [W/ m K]	3.68×10^{-2}	4.27×10^{-2}
Argon kinematic viscosity ν_{Ar} [m^2 /s]	7.67×10^{-5}	1.11×10^{-4}

$$\frac{\partial T_l(x,\,t)}{\partial t} = \alpha_l \frac{\partial^2 T_l(x,\,t)}{\partial x^2} \text{for} \, x > S(t),\; t > 0 (\text{liquid phase}) \tag{A.2}$$

$$\frac{dT_s(x,\,t)}{dt} = \alpha_s \frac{\partial^2 T_s(x,\,t)}{\partial x^2} \text{for} \, 0 < x < S(t),\; t > 0 \,(\text{solid phase}) \tag{A.3}$$

At the liquid/solid interface the energy balance yields:

$$k_s \frac{\partial T_s(x,\,t)}{\partial x} - k_l \frac{\partial T_l}{\partial x} = \rho L \frac{dS}{dt} \text{for} \, x = S(t) \tag{A.4}$$

where α_l, α_{ls}, k_l, k_s are the thermal diffusivity and the thermal conductivity of the liquid and solid phase (Sn and Ag respectively), and S(t) is the moving solidification front. Applying the following boundary conditions:

$T_l(x,\,t) = T_s(x,\,t) = T_m$ (constant) at $x = S(t),\; t > 0$

$T_s(x,\,t) = T_{sub}$ (constant) for $x = -\infty,\; t > 0$

$T_l(x,\,t) = T_{drop}$ (constant) for $x = +\infty,\; t > 0$

The Neumman's analytical solution for the solidification front is given by Eq. (A.5):

$$S(t) = [k_s \frac{(T_m - T_{sub})e^{-\lambda^2}}{\sqrt{\alpha_s}\,[1 + \text{erf}(\lambda)]} + k_l \frac{(T_m - T_d)e^{\frac{-\alpha_s \lambda^2}{\alpha_l}}}{erfc(\lambda\sqrt{\frac{\alpha_s}{\alpha_l}})}] \frac{2\sqrt{t}}{\rho L \sqrt{\pi}} \tag{A.5}$$

while the temperature profiles and distributions in the liquid and solid phase are:

$$T_l(x,\,t) = T_{drop} - (T_{drop} - T_m)\frac{\text{erf}(\frac{x}{2\sqrt{\alpha_l t}})}{\text{erf}(\lambda)} \tag{A.6}$$

$$T_s(x,\,t) = T_{sub} + (T_m - T_{sub})\frac{\text{erfc}\left(\frac{x}{2\sqrt{\alpha_s t}}\right)}{\text{erfc}\left(\lambda\sqrt{\alpha_l/\alpha_s}\right)} \tag{A.7}$$

where λ relates to the initial conditions of the problem and is derived iteratively from the solution of following transcendental Eq. (A.8):

$$\frac{St_l}{e^{\lambda^2}\text{erf}(\lambda)} - \frac{St_s\sqrt{\alpha_s}}{\sqrt{\alpha_l}e^{\frac{\alpha_l\lambda^2}{\alpha_s}}erfc\left(\lambda\sqrt{\alpha_l/\alpha_s}\right)} = \lambda\sqrt{\pi} \tag{A.8}$$

By equating the heat flux of the droplet and substrate the initial liquid/substrate interface temperature T_i is obtained as per Eq. (A.9):

$$T_i = \frac{T_{drop}\sqrt{\rho_l k_l c_l} + T_{sub}\sqrt{\rho_s k_s c_s}\,\text{erf}(\lambda)}{\sqrt{\rho_l k_l c_l} + \sqrt{\rho_s k_s c_s}\,\text{erf}(\lambda)} \tag{A.9}$$

This expression can be used to calculate the approximate instantaneous droplet/substrate interfacial temperature as a function of the initial impinging droplet temperature and temperature of the substrate and therefore can be used to create process maps to obtain desired substrate re-melting. Fig. A1 shows the combination of droplet impinging and substrate temperatures that produce an interface temperature equal to the melting point of Sn and Ag and the black diamond marker indicates the process condition adopted in the present research. Assuming that to ensure droplet re-melting the interface needs to reach the melting point of the material, this simple approximation corroborates the microscopy evidence that Ag droplets have not enough thermal energy to re-melt the droplet interface, explaining the lack of metallurgical bonding observed across contiguous droplets. Additional research to improve the printing process by dispensing droplets that imping the substrate at higher temperatures or by *in-situ* sintering is on-going [33].

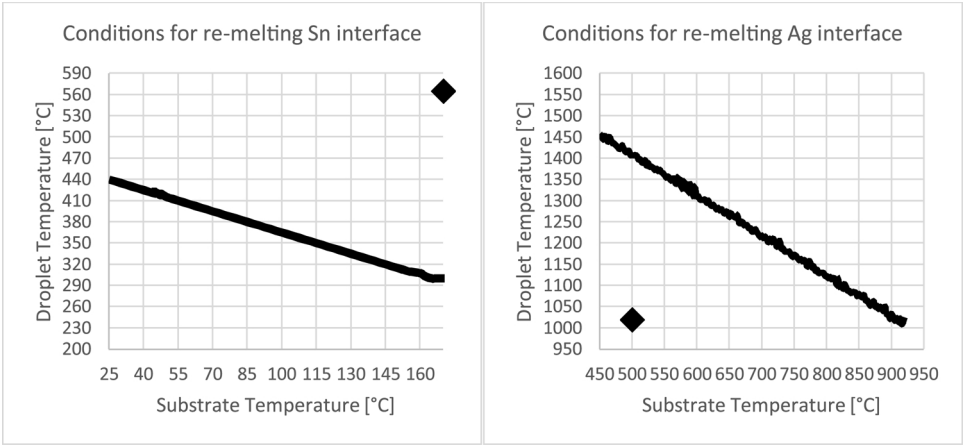

Fig. A1. Combination of impinging droplet and substrate temperature which generate an interface temperature T_i equal to the melting point of (a) Sn and (b) Ag. The diamond marker shows the calculated average T_i obtained in the Sn and Ag experiments.

Appendix B. Supplementary data

Supplementary material related to this article can be found, in the online version, at doi:https://doi.org/10.1016/j.addma.2019.100930.

References

[1] W.J. Sames, F.A. List, S. Pannala, R.R. Dehoff, S.S. Babu, The metallurgy and processing science of metal additive manufacturing, Int. Mater. Rev. 61 (5) (2016) 315–360.

[2] L.E. Murr, W.L. Johnson, 3D metal droplet printing development and advanced materials additive manufacturing, J. Mater. Res. Technol. 6 (1) (2017) 77–89.

[3] W.A. Harkness, J.H. Goldschmid, Free-Form Spatial 3-D Printing Using Part Levitation, Google Patents, 2016.

[4] Q. Liu, M. Orme, High precision solder droplet printing technology and the state-of-the-art, J. Mater. Process. Technol. 115 (3) (2001) 271–283.

[5] T. Lee, T.G. Kang, J. Yang, J. Jo, K. Kim, B. Choi, D. Kim, Drop-on-Demand solder droplet jetting system for fabricating microstructure, Ieee Trans. Electron. Packag. Manuf. 31 (3) (2008) 202–210.

[6] M. Orme, R.F. Smith, Enhanced aluminum properties by means of precise droplet deposition, J. Manuf. Sci. Eng. 122 (3) (1999) 484–493.

[7] S.X. Cheng, T. Li, S. Chandra, Producing molten metal droplets with a pneumatic droplet-on-demand generator, J. Mater. Process. Technol. 159 (3) (2005) 295–302.

[8] F. Ming, C. Sanjeev, P.C. B, Building three-dimensional objects by deposition of molten metal droplets, Rapid Prototyp. J. 14 (1) (2008) 44–52.

[9] N. Lass, L. Riegger, R. Zengerle, P. Koltay, Enhanced liquid metal Micro droplet generation by pneumatic actuation based on the StarJet method, Micromachines 4 (1) (2013) 49–66.

[10] Z. Luo, X. Wang, L. Wang, D. Sun, Z. Li, Drop-on-demand electromagnetic printing of metallic droplets, Mater. Lett. 188 (2017) 184–187.

[11] M. Suter, E. Weingärtner, K. Wegener, MHD printhead for additive manufacturing of metals, Procedia Cirp 2 (2012) 102–106.

[12] Y. Oh, V. Bharambe, B. Mummareddy, J. Martin, J. McKnight, M.A. Abraham, J.M. Walker, K. Rogers, B. Conner, P. Cortes, E. MacDonald, J.J. Adams, Microwave dielectric properties of zirconia fabricated using NanoParticle Jetting™, Addit. Manuf. 27 (2019) 586–594.

[13] J. Vaithilingam, M. Simonelli, E. Saleh, N. Senin, R.D. Wildman, R.J.M. Hague, R.K. Leach, C.J. Tuck, Combined inkjet printing and infrared sintering of silver nanoparticles using a swathe-by-swathe and layer-by-layer approach for 3-dimensional structures, ACS Appl. Mater. Interfaces 9 (7) (2017) 6560–6570.

[14] A.A. Tseng, M.H. Lee, B. Zhao, Design and operation of a droplet deposition system for freeform fabrication of metal parts, J. Eng. Mater. Technol. 123 (1) (1999) 74–84.

[15] Y. Idell, N. Watkins, A. Pascall, J. Jeffries, K. Blobaum, Microstructural characterization of pure tin produced by the drop-on-demand technique of liquid metal jetting, Metall. Mater. Trans. A 50 (9) (2019) 4000–4005.

[16] M. Orme, R.F. Smith, Enhanced aluminum properties by means of precise droplet deposition, J. Manuf. Sci. Eng. 122 (3) (2000) 484–493.

[17] W. Cao, Y. Miyamoto, Freeform fabrication of aluminum parts by direct deposition of molten aluminum, J. Mater. Process. Technol. 173 (2) (2006) 209–212.

[18] V. Sukhotskiy, P. Vishnoi, I.H. Karampelas, S. Vader, Z. Vader, E.P. Furlani, Magnetohydrodynamic drop-on-demand liquid metal additive manufacturing: system overview and modelling, 5th International Conference of Fluid Flow, Heat and Mass Transfer (FFHMT'18), Niagra Falls, Canada, 2018.

[19] V. Sukhotskiy, I.H. Karampelas, G. Garg, A. Verma, M. Tong, S. Vader, Z. Vader, E.P. Furlani, Magnetohydrodynamic Drop-On-Demand Liquid Metal 3D Printing Solid Freeform Fabrication Symposium Austin, Texas, US (2017).

[20] S. Vader, Z. Vader, I.H. Karampelas, E.P. Furlani, Magnetohydrodynamic Liquid Metal Jet Printing, Advanced Manufacturing, Electronics, and Microsystems, (2015).

[21] K.Z. Dinesh Krishna Kumar Jayabal, D. Cormier, fabrication of support-less engineered lattice structures via jetting of molten aluminium droplets solid freeform fabrication, Proceedings of the 29th Annual International, Austin, Texas, 2018.

[22] R.B. Mircea Rasa, W. Classens, H.V. Genuchten, E. Kuznetsov, O.-T. B.V (Ed.), Device for Ejecting Droplets of a Fluid Having a High Temperature, 2013.

[23] E. MacDonald, R. Wicker, Multiprocess 3D printing for increasing component functionality, Science 353 (6307) (2016) aaf2093.

[24] W. Chien-Hsun, T. Ho-Lin, W. Yu-Che, H. Weng-Sing, Investigation of molten metal droplet deposition and solidification for 3D printing techniques, J. Micromechanics Microengineering 26 (9) (2016) 095012.

[25] C.-H. Wang, H.-L. Tsai, W.-S. Hwang, Direct printing of 1-D and 2-D electronically conductive structures by Molten lead-free solder, Materials 10 (1) (2017).

[26] S. Schiaffino, A.A. Sonin, Molten droplet deposition and solidification at low Weber numbers, Phys. Fluids 9 (11) (1997) 3172–3187.

[27] J. Gong, C. Liu, P.P. Conway, V.V. Silberschmidt, Evolution of CuSn intermetallics between molten SnAgCu solder and Cu substrate, Acta Mater. 56 (16) (2008) 4291–4297.

[28] M. Fang, S. Chandra, C.B. Park, Building three-dimensional objects by deposition of molten metal droplets, Rapid Prototyp. J. 14 (1) (2008) 44–52.

[29] C.W. Visser, R. Pohl, C. Sun, G.-W. Römer, B. Huis in 't Veld, D. Lohse, 3D printing: toward 3D printing of pure metals by laser-induced forward transfer (Adv. Mater. 27/2015), Adv. Mater. 27 (27) (2015) 4103-4103.

[30] H.W. Sheng, G. Wilde, E. Ma, The competing crystalline and amorphous solid solutions in the Ag–Cu system, Acta Mater. 50 (3) (2002) 475–488.

[31] H.H.a.S.A. Argyropoulos, Mathematical modelling of solidification and melting: a review, Model. Simul. Mat. Sci. Eng. 4 (1996) 371–396.

[32] C.T.R. Hague, Y. Shikhmurzaev, J. Sprittles, R. Wildman, C. Roberts, I. Ashcroft, M. Fromhold, Enabling Next Generation Additive Manufacturing, EPSRC, 2017.

[33] D.I. Richard Hague, Christopher Tuck, Yuli Shikhmurzaev, James Sprittles, Ricky Wildman, Clive Roberts, Ian Ashcroft, Mark Fromhold, Enabling Next Generation Additive Manufacturing, EPSRC, University of Nottingham, University of Birmingham, University of Warwick, (2017).